# Three-Dimensional-Topological-Insulator Tunnel Diodes

Stephen P. Fluckey,[1] Sabyasachi Tiwari,[2,3,4] Christopher L. Hinkle,[5] and William G. Vandenberghe[2,*]

[1] *Department of Physics, The University of Texas at Dallas, 800 West Campbell Road, Richardson, Texas 75080, USA*

[2] *Department of Materials Science and Engineering, The University of Texas at Dallas, 800 West Campbell Road, Richardson, Texas 75080, USA*

[3] *Department of Materials Engineering, KU Leuven, Kasteelpark Arenberg 44, Leuven 3001, Belgium*

[4] *Imec, Kapeldreef 75, Heverlee 3001, Belgium*

[5] *Department of Electrical Engineering, The University of Notre Dame, Notre Dame, Indiana 46556, USA*

(Received 2 March 2022; revised 12 July 2022; accepted 20 October 2022; published 13 December 2022)

Topological insulators (TIs) open up many avenues for designing future electronic devices. Using the Bardeen transfer Hamiltonian method, we calculate the current density of electron tunneling between two slabs of $Bi_2Se_3$. We calculate the three-dimensional TI tunnel-diode current-voltage ($J$-$V$) characteristics for different doping concentrations, tunnel-barrier heights and thicknesses, and 3D-TI band gaps. The difference in the Fermi levels of the slabs determines the peak and valley voltages. The tunnel-barrier width and height affect the magnitude of the current without affecting the shape of the $J$-$V$ characteristics. The band gap of the 3D TI determines the magnitude of the tunnel current, albeit at a lesser rate than the tunnel-barrier potential; thus the device characteristics are robust under changing TI material. The high peak-to-valley ratio of 3D-TI tunnel diodes, the controllability of the valley-current location, and the simple construction provide advantages over other negative-differential resistance devices.

DOI: 10.1103/PhysRevApplied.18.064037

## I. INTRODUCTION

Topological insulators (TIs) are a class of material with spin-momentum-locked surface or edge states. TIs are classified as either two-dimensional (2D) or three-dimensional (3D). A 2D TI has an insulating 2D bulk and a conducting edge, while a 3D TI has an insulating bulk and conducting surface. 3D TIs are arguably more promising for short-term device applications than 2D TIs, because well-known materials such as $Bi_2Se_3$ are 3D TIs, while 2D TIs rely on more exotic materials [1], such as stanene [2,3] and bismuthene [4].

In $Bi_2Se_3$ and related TIs, spin-orbit interactions lead to the quantum spin Hall effect, which is associated with an insulating bulk and conducting gapless edge states. Specifically for 3D TIs such as $Bi_2Se_3$, if the energy of the spin-orbit coupling is larger than some critical value, the order between two energy levels nearest to the Fermi energy is reversed. Because these two energy levels have an opposite parity, this drives the system into a TI phase [5].

Surface states of 3D TIs have the interesting property that they have a Dirac dispersion and that their spin and momentum is locked [6]. Previous device proposals have exploited the spin-momentum locking to convert charge to spin [7]. Here, we take a different approach and exploit the spin-momentum locking of 3D-TI surface states to block the tunneling current and realize a negative-differential resistance (NDR) device [8].

Recent advances in the field of TIs [9] have opened up a plethora of opportunities for their use in both charge-based [1,6] and spin-based devices [10,11]. TIs have been proposed for many exotic applications, including quantum computation [12], lasing [13], and skyrmion-based devices [14]. Some recent proposed applications are electrochemical energy storage [15] and mode-locked lasers [16]. Electric-field control of the surface state spin-polarization opens up a plethora of opportunities in building spin-based devices using $Bi_2Se_3$, including superconductivity [17], photodetectors [18], and tetrahertz frequency generation [19].

NDR devices are a class of electronic devices with nonlinear current-voltage ($J$-$V$) characteristics. Specifically, they have regions in which their current decreases with increasing voltage. Due to their unusual response to applied voltage, they are used in many applications such as fast memories, high-frequency devices, frequency multipliers, and fast switching devices [20].

*Email: william.vandenberghe@utdallas.edu

 

Unfortunately, present-day NDR devices are less controllable in terms of the location of the minima and come with a fixed peak-to-valley ratio [21], which is the ratio of the maximum current to that of the current at the minimum. Although some devices based on nanoscale molecular junctions [22] and graphene nanoribbons [23] have been proposed to remedy the relatively little control possessed in many current NDR devices, the difficulty in fabricating such devices presents a roadblock for their practical application [24,25]. The difficulty in fabricating 2D NDR devices has been noted in both graphene nanoribbons [24] and graphene quantum dots [26]. The development of a 3D-TI NDR device could potentially solve many of these issues.

In this work, we investigate a two-terminal NDR device using two 3D-TI slabs separated by a tunnel barrier. First, we model the electronic structure of 3D TIs and present the theoretical formulation for calculating the tunneling current. We then show the NDR characteristics of the proposed device and discuss various control parameters, such as device geometry and TI material selection, which can be tuned to control the characteristics of the device. We show that the presented device provides a very high peak-to-valley ratio along with an efficient control over the position of the valley current, the location of the minimum of the current in the NDR region. Finally, we discuss the results and their implications and conclude.

## II. DEVICE STRUCTURE AND THEORETICAL MODEL

### A. Device structure

Figure 1(a) shows the schematic of the $Bi_2Se_3$ device under investigation. The device is comprised of two TIs separated by a tunnel barrier. The two slabs of $Bi_2Se_3$ are assumed to have different Fermi levels, as determined by their doping [27,28]. We choose $Bi_2Se_3$ because it is the most studied 3D TI but our findings apply to any material with a spin-polarized Dirac cone and $\mathbb{Z}_2$ topological order. The spin-polarized conducting surface states are illustrated by the surfaces of the two slabs. The top and bottom slabs are given different colors in our schematic to reference the difference in the Fermi levels ($\Delta E_F$) of the two slabs shown in Fig. 1(b).

The top slab, which is $p$ doped, is connected to a voltage source to set the bias $V_{pn}$ and the bottom slab, which is $n$ doped, is grounded. The total device thickness in our simulations is taken to be 21 nm with a slab size of 10 nm for the $p$-doped and the $n$-doped slabs and a tunnel-barrier thickness of 1 nm. The layered nature of our device allows the thickness of the tunnel barrier to be controlled. Translational symmetry is assumed in the transverse $x$ and $y$ directions.

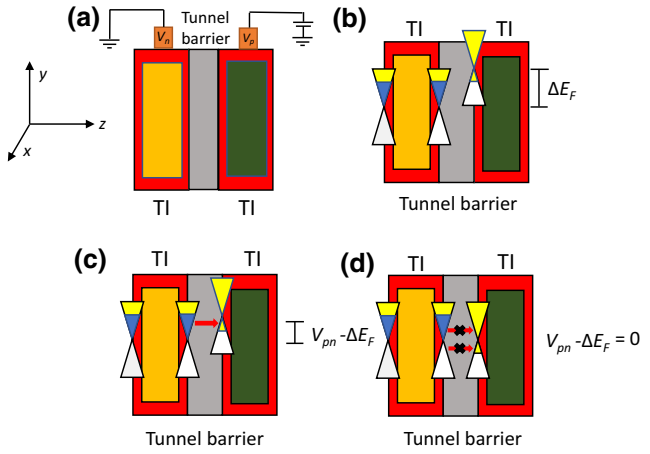


FIG. 1. (a) The device schematic for our proposed TI-tunnel-diode NDR device. The top slab (green) is $p$ doped and connected to bias, while the bottom slab (yellow) is $n$ doped and grounded. The $p$-doped and $n$-doped slabs have thickness $t_p = t_n = 10$ nm. The default thickness of the tunnel barrier is $t = 1.0$ nm. (b) The relative position of the TI slab Dirac cones due to $\Delta E_F$ at zero bias. (c) The relative position of the TI slab Dirac cones at bias $V_{pn} < \Delta E_F$, where a finite tunneling current is present between the TI slabs. (d) The relative position of the TI slab Dirac cones at bias $V_{pn} = \Delta E_F$, where spin polarization prevents tunneling between the TI slabs.

### B. Device operation

Figures 1(b)–1(d) illustrate the position of the Dirac cones of the surface states of both the slabs at different applied bias ($V_{pn}$). Figure 1(b) shows the Dirac cones when no bias is applied ($V_{pn} = 0$). In Fig. 1(c), the Dirac cone of the top slab shifts down due to an applied bias $0 < V_{pn} < \Delta E_F$. With an applied bias, a finite tunneling current flows between the slabs, as indicated by the red arrow. The tunneling occurs between the surface states of the $n$-doped and $p$-doped slabs. Figure 1(d) shows the case when the applied bias equals the Fermi-level difference ($V_{pn} = \Delta E_F$); the Dirac cones of the surface states now match perfectly. However, the surface states have opposite spin-momentum locking, which will make the tunneling current vanish. Momentum and energy can be conserved but spin cannot be conserved because of the opposite spin-polarization of both surface states. A more detailed examination of the effects of spin-polarized surface states on the tunneling current is presented in Sec. III A.

In Sec. III B, we show how this device responds to changes to key device parameters. We first examine how properties of the tunnel barrier, specifically the width and potential or 'height' of the tunnel barrier, both of which can be simply controlled, affect device performance. We also show how the effects on the Fermi level through doping affect device performance. Finally, we examine the effects of changing the TI material, which can also model how chemical or mechanical strain on $Bi_2Se_3$ might impact device behavior.

### C. Electronic structure of slabs

We model the TIs and the tunnel barriers using a $\mathbf{k}\cdot\mathbf{p}$ Hamiltonian to describe the TI device performance. We use the $Bi_2Se_3$ Hamiltonian from Ref. [29]:

$$H(\mathbf{k}) = \epsilon_0(\mathbf{k})\mathcal{I} + \begin{pmatrix} \mathcal{M}(\mathbf{k}) & A_1k_z & 0 & A_2k_- \\ A_1k_z & -\mathcal{M}(\mathbf{k}) & A_2k_- & 0 \\ 0 & A_2k_+ & \mathcal{M}(\mathbf{k}) & -A_1k_z \\ A_2k_+ & 0 & -A_1k_z & -\mathcal{M}(\mathbf{k}) \end{pmatrix}, \tag{1}$$

where $k_\pm = k_x \pm ik_y$, $\epsilon_0(\mathbf{k}) = C + D_1k_z^2 + D_2(k_x^2 + k_y^2)$, $\mathcal{I}$ is a $4\times4$ identity matrix, and $\mathcal{M}(\mathbf{k}) = M - B_1k_z^2 - B_2(k_x^2 + k_y^2)$. The directions $x$ and $y$ are defined as being in plane with the TI surface. The $z$ direction is defined as being the out-of-plane direction. $k_x$, $k_y$, and $k_z$ are the wave-vector components in the $x$, $y$, and $z$ directions. This Hamiltonian keeps terms up to quadratic order in $\mathbf{k}$.

The biases under study for our device range from 0.0 eV to 0.2 eV. This range of energies only requires that we consider the low-energy behavior of our TI Hamiltonian. This low-energy Hamiltonian accurately models the ground and first excited energy eigenstates of our TI device [30], which is sufficient to accurately model the $J$-$V$ curves of our device, as the topological nature of $Bi_2Se_3$ is determined by the physics near the $\Gamma$-point. In Sec. A 2, we show that considering only the ground- and first-excited-state energy eigenstates is sufficient to accurately model the device behavior. The eigenvalues of this Hamiltonian display rotational symmetry in the transverse directions $k_x$ and $k_y$ in this low-energy approximation.

The parameters $B_1$, $B_2$, $C$, $D_1$, $D_2$, and $M$ are presented in Table I in Sec. A 1 and have previously been determined for $Bi_2Se_3$ in Ref. [29] by fitting to the bulk $Bi_2Se_3$ band structure obtained from *ab initio* density-functional theory calculations. These parameters give us the slab Hamiltonian $H_{\mathrm{TI},p}$ and $H_{\mathrm{TI},n}$.

We use vacuum as the interface tunnel barrier, as $Bi_2Se_3$ is a van der Waals material. To model the Hamiltonian of this tunnel barrier, $H_T$, we set the parameters to those of a free electron with a 1-eV on-site potential [6] to mimic a tunnel barrier with a 1-eV barrier. The parameters $D_1 = D_2 = 3.8$ eV A$^2 = \hbar^2/(2m_e)$, where $\hbar$ is the reduced Planck constant, are chosen to give the electron the free electron mass in the tunnel barrier.

Any material that has a barrier mismatch could, in principle, be used as a tunnel barrier for this device. Since the TI has surface states and a significant amount of charge on the surface, we assume that the entire voltage is dropped over the tunnel barrier. Gapped van der Waals materials such as transition-metal dichalcogenides (TMDs) are ideal because of the of lack of dangling bonds, making defect formation less likely.

To apply a Fermi shift of $\Delta E_F$, we add a term $\Delta E_F$ to the diagonal elements of the Hamiltonian in Eq. (1). We apply a bias by subtracting $V_{pn}$ from $\Delta E_F$ and treating this as the new effective Fermi shift for $H_{\mathrm{TI},p}$.

In Fig. 2, we show the band structure of a TI slab. The left-hand side of Fig. 2 represents the bottom $n$-doped slab without any Fermi-level shift, while the right-hand side represents the top $p$-doped slab with a Fermi-level shift of 0.10 eV at zero applied bias. The $p$-doped and $n$-doped Fermi levels are represented by dotted lines. The opposite spin polarizations are represented by red and green shading. It can be observed that doping creates a difference between the $p$-doped and $n$-doped Fermi levels. We obtain the topological surface states by solving our model Hamiltonian with an open boundary condition [31]. To compute the wave functions in the out-of-plane direction, $z$, we convert $k_z$ to $i(d/dz)$, and discretize the Hamiltonian in Eq. (1) using finite differences, as detailed in Sec. A 1. The spin-polarized surface states of the top and bottom

TABLE I. The $\mathbf{k}\cdot\mathbf{p}$ parameters for $Bi_2Se_3$ [29] and the tunnel barrier. These values are used unless noted otherwise.

| Parameter | $Bi_2Se_3$ | Tunnel barrier |
|---|---|---|
| $M$ | 0.28 eV | 0 eV |
| $A_1$ | 2.2 eV A | 0 eV A |
| $A_2$ | 4.1 eV A | 0 eV A |
| $B_1$ | 10 eV A$^2$ | 0 eV A$^2$ |
| $B_2$ | 56.6 eV A$^2$ | 0 eVA$^2$ |
| $C$ | -0.0068 eV | 1 eV |
| $D_1$ | 1.3 eV A$^2$ | 3.8 eV A$^2$ |
| $D_2$ | 19.6 eV A$^2$ | 3.8 eV A$^2$ |

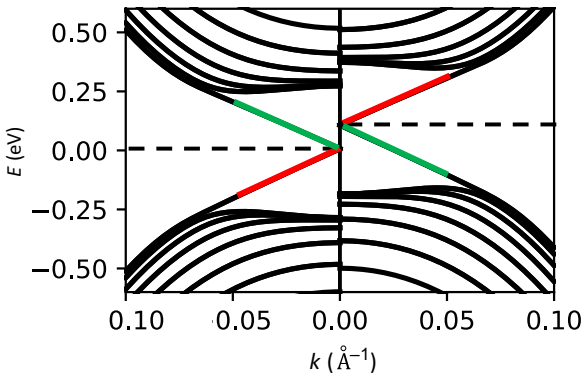


FIG. 2. The band structure of a TI slab of 10-nm thickness plotted in the transverse direction, $k = \sqrt{k_x^2 + k_y^2}$. The left-hand side corresponds to the $n$-doped TI slab of Fig. 1(b) and has no Fermi-level shift, while the right-hand side corresponds to the $p$-doped TI slab of Fig. 1(b) and has a Fermi-level shift $\Delta E_F$ of 0.1 eV. The dotted lines represent the effective Fermi level of the $p$-doped and $n$-doped slabs with this Fermi-level shift. The red and green shading represents the spin-polarized region of the surface bands: red coloration represents one spin polarization, while the green represents the opposite polarization.

slabs have different energies because of the 0.1-eV relative Fermi-level difference.

### D. Tunneling current

We use the Bardeen transfer Hamiltonian method [32] to calculate the tunneling current between the TI slabs. The Bardeen transfer Hamiltonian follows from time-dependent perturbation theory [33], which treats the Hamiltonian of the intervening barrier as a perturbation. We sum over the intersecting pairs of bands $\mu_j$ and $\eta_j$ with band index $j$. By integrating over the one-dimensional first Brillouin zone and by requiring energy conservation, the current is determined by the intersection of $E_{p\mu}(k)$ and $E_{n\eta}(k)$. Here, we express the band energies of these bands in terms of $k$ by making the substitution $k_+k_- = k^2$. Summing over pairs of intersecting bands with index $\mu$ and $\eta$ leads to the probability of transition between the $p$-doped and $n$-doped slabs:

$$P = \frac{2\pi}{\hbar}\sum_j \int\int \frac{dk_x}{2\pi}\frac{dk_y}{2\pi}|M_j|^2\delta(E_{n\mu_j}(k) - E_{p\eta_j}(k)), \tag{2}$$

where

$$|M_j| = \left|\Psi_{n\mu_j}(\kappa_j)\frac{d\Psi_{p\eta_j}(\kappa_j)}{dz} - \Psi_{p\eta_j}(\kappa_j)\frac{d\Psi_{n\nu_j}(\kappa_j)}{dz}\right| \tag{3}$$

is the transition-matrix element corresponding to the transition between the wave functions of bands $E_{p\mu}(k)$ and $E_{n\eta}(k)$ for $k = \sqrt{k_x^2 + k_y^2}$.

Since our Hamiltonian exhibits in-plane rotational symmetry, we convert to a polar coordinate system where $k_x = k\cos(\theta)$ and $k_y = k\sin(\theta)$. We use $k^2 = k_x^2 + k_y^2$ and $dk_xdk_y = kdkd\theta$ to arrive at

$$P = \frac{1}{\hbar}\sum_j \int kdk|M_j|^2\delta(E_{n\mu_j} - E_{p\eta_j}). \tag{4}$$

Since our TI Hamiltonian exhibits rotational symmetry and thus its eigenvalues can be written as being dependent only on $k$, we can straightforwardly convert the delta function as a function of energy in Eq. (4) to be a function of $k$. We integrate over the first Brillouin zone and require energy conservation. To integrate over $k$, we change $\delta(E_{p\mu} - E_{n\eta})$ to a function of $k$ using $\delta(E_{n\mu} - E_{p\eta}) = \delta(k_{n\mu} - k_{p\eta})\left|d((E_{p\mu}(k)) - (E_{n\eta}(k)))/dk\right|^{-1}$.

We evaluate the integral in Eq. (4):

$$P = \frac{1}{\hbar}\sum_j \kappa_j \left|\frac{d(E_{p\mu_j}(k) - E_{n\eta_j}(k))}{dk}\right|^{-1}_{k=\kappa_j}|M_j|^2, \tag{5}$$

where $\kappa_j$ is the $k$ value at the intersection point.

To model the current density resulting from this transmission probability, we multiply by the electron charge $q$ and the difference in the Fermi-Dirac distribution functions $f(E_n) - f(E_p)$:

$$J = \frac{q}{\hbar}\sum_j \kappa_j|M_j|^2\left|\frac{d(E_{p\mu_j}(k) - E_{n\eta_j}(k))}{\mathrm{d}k}\right|^{-1}_{k=\kappa_j}(f(E_{p\mu_j}(\kappa_j) - V_{pn}) - f(E_{n\eta_j}(\kappa_j))) \tag{6}$$

where $V_p$ and $V_n$ are the $n$-doped and $p$-doped voltages, respectively, the difference of which is $V_{pn}$.

We use 4500 $k$ points to calculate the band structure of the slabs. We take a step size of $\Delta z = 1$ Å. We model the performance of our TI device at room temperature. We consider the eight energy bands closest to the Fermi level in the calculation of the current, as these bands give the largest contribution to the tunneling current. Because of the bands considered, we only encounter, at most, one intersection between any two bands. In the case of multiple intersections, a summation over a different $\kappa$ would be required. Calculating additional bands gives additional possibilities for tunneling and thus increases the current but this increase does not change the shape of the $J$-$V$ curves and the increase in the magnitude of the current density quickly becomes negligible. A more detailed examination of the change in the current that results from calculating additional bands can be seen in Sec. A 2.

## III. RESULTS AND DISCUSSION

### A. Current density

Figure 3 shows the calculated current density $J$ as a function of $V_{pn}$ with Fermi-level shifts ($\Delta E_F$) of 0.05 eV, 0.10 eV, and 0.15 eV on the $p$-doped slab. These Fermi-level shifts characterize how changing the doping of the TI slabs affects the device behavior. We observe that the current initially increases linearly with the applied $V_{pn}$. However, at $V_{pn} \approx \Delta E_F/3$, the current peaks and starts to

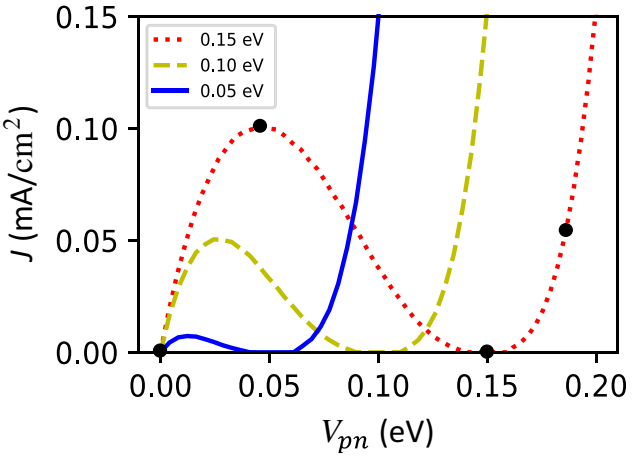


FIG. 3. The current density of our proposed TI NDR device with Fermi-level shift $\Delta E_F = 0.05$ eV, $\Delta E_F = 0.10$ eV, and $\Delta E_F = 0.15$ eV. The valley-current location on the $J$-$V$ curve is determined by the Fermi level of the $p$-doped slab. The black dots represent bias points for which the band structure and wave functions are calculated in Fig. 4.

decrease and goes to almost zero at $V_{pn} = \Delta E_F$, resulting in NDR behavior. Interestingly, we find that unlike conventional NDR devices, the valley current of which remains finite [21], because of the very small valley current, the peak-to-valley ratio is very high. For bias $V_{pn} > \Delta E_F$, the current starts to increase again. We also observe from Fig. 3 that the maximum current and the valley bias are both determined by the difference in the Fermi level between the TI slabs.

To further analyze the device characteristics, we show the band structure and the wave function of the $p$-doped and the $n$-doped TI slab at $V_{pn} = 0$ eV, 0.05 eV, 0.15 eV, and 0.18 eV in Figs. 4–7, respectively. We choose $\Delta E_F = 0.15$ eV, which corresponds to the red dotted curve in Fig. 3. The wave functions on the right are calculated at an intersection point between the two bands for each bias point.

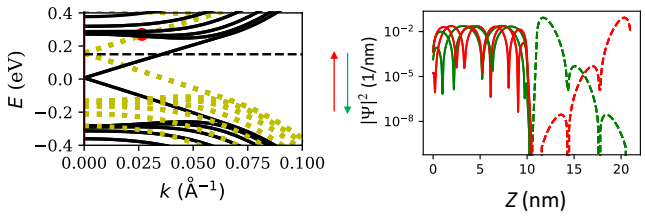


FIG. 4. The band structure of $Bi_2Se_3$ for applied bias $V_{pn} = 0.0$ eV corresponding to the first dot in Fig. 3. The solid black line represents the $n$-doped slab and the dotted yellow line represents the $p$-doped slab. The red dot indicates a chosen intersection for consideration with the wave functions calculated at that intersection point plotted to the right. Here, we have an intersection between a bulk state and an edge state and no current.

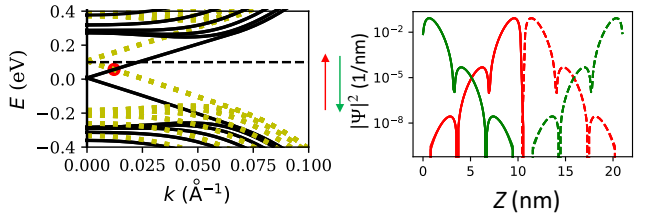


FIG. 5. The band structure of $Bi_2Se_3$ for applied bias $V_{pn} = 0.05$ eV corresponding to the second dot in Fig. 3. The solid black line represents the $n$-doped slab and the dotted yellow line represents the $p$-doped slab. The red dot indicates a chosen intersection for consideration, with the wave functions calculated at that intersection point are plotted to the right. Here, we have two same-spin surface-state intersections and a finite tunneling current.

Figure 4 shows the band structure and the wave functions at $V_{pn} = 0$ eV. This corresponds to the first black dot in Fig. 3 Although there are states available for tunneling, the zero bias causes the tunneling current to remain zero (first black dot in Fig. 3).

Figure 5 shows the band structure and the wave functions at a bias $V_{pn} = 0.05$ eV, which corresponds to the second black dot in Fig. 3. We now have two same-spin surface states intersecting, shown by the red dot in Fig. 5 (band structure). We see that the wave functions of the same spin overlap result in a finite tunneling current. We see in Fig. 3 that the tunneling current increases from zero bias up until a bias that is approximately one third of the Fermi-level difference between the two slabs.

Figure 6 shows the band structure and the wave functions at a bias $V_{pn} = 0.15$ eV. This corresponds to the third black dot in Fig. 3. Now, we have two opposite-spin surface states intersecting. Although the wave functions of the top and the bottom slab have a significant spatial overlap, their opposite spin causes the tunneling current to become very low (as shown in the third black dot in Fig. 3), resulting in a very low valley current for the device.

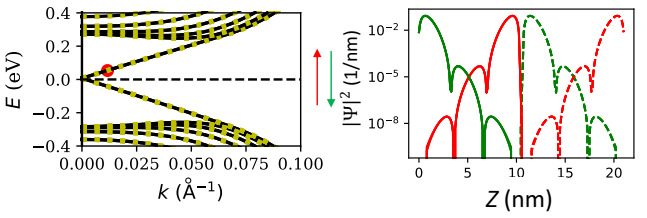


FIG. 6. The band structure of $Bi_2Se_3$ for applied bias $V_{pn} = 0.15$ eV corresponding to the third dot in Fig. 3. The solid black line represents the $n$-doped slab and the dotted yellow line represents the $p$-doped slab. The red dot indicates a chosen intersection, for consideration with the wave functions calculated at that intersection point plotted to the right. Here, we have two opposite-spin surface-state intersections and a nearly zero tunneling current.

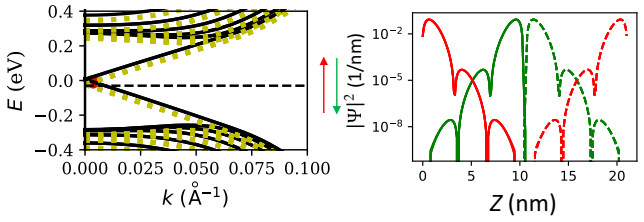


FIG. 7. The band structure of $Bi_2Se_3$ for applied bias $V_{pn} = 0.18$ eV corresponding to the fourth dot in Fig. 3. The solid black line represents the $n$-doped slab and the dotted yellow line represents the $p$-doped slab. The red dot indicates a chosen intersection for consideration, with the wave functions calculated at that intersection point plotted to the right. Here, we have two same-spin surface-state intersections and a finite tunneling current.

Figure 7 shows the band structure and the wave functions at a bias $V_{pn} = 0.18$ eV. This corresponds to the final black dot in Fig. 3. We see that the wave functions of the same spin overlap, resulting in a finite tunneling current.

To quantify the overlap, we inspect the transition element for different bias conditions. For a bias of 0.05 eV, the transition element $|M|^2 = 2.32 \times 10^6$ $(\text{eV})^2$. At the point where $V_{pn} = \Delta E_F = 0.15$ eV, the transition element is significantly lower at $|M|^2 = 1.10$ $(\text{eV})^2$. At $V_{pn} = 0.18$ eV, significantly larger than $\Delta E_F$, the transition element has once again increased, to be on the same order as for 0.05-eV bias at $|M|^2 = 1.76 \times 10^6$ $(\text{eV})^2$. The transition element in the case of $V_{pn} = 0.18$ eV, being lesser, gives rise to a lower current as compared to $V_{pn} = 0.05$ eV, as can be seen in comparing the values of the current at the second and fourth black dots in Fig. 3. Both $V_{pn} = 0.05$ eV and 0.18 eV have a significantly higher $M$ value than the value at $V_{pn} = \Delta E_F$.

### B. Parametric device analysis

When studying the NDR tunneling current, there are several parameters of interest. The first of these parameters is the relative Fermi level of the two slabs. The second and third parameters are the barrier height and barrier thickness. The final parameter is the band gap of the slabs, the range of energy between the surface states and the first bulk states.

Figure 8(a) shows the current density as a function of the applied bias for tunnel-barrier thickness $t = 1.0$ nm, $t = 1.5$ nm, and $t = 2.0$ nm. The shape of the current density remains the same, as do the biases at which the peak and valley currents occur. However, as the thickness of the tunnel barrier between the slabs increases, the magnitude of the current rapidly decreases. This is expected, as increasing the gap between the TI slabs decreases the tunneling probability.

Figure 8(b) shows the current density for the tunnel barrier on-site potentials $V_{\text{onsite}} = 1$ eV, 1.1 eV, and 1.2 eV. The magnitude of the current density decreases with an increasing tunnel barrier on-site potential. The increasing potential increases the tunnel barrier. Since the TIs are unaltered, only the magnitude is affected, not the shape of the $J$-$V$ curve.

Figure 8(c) shows how the current density changes when the TI band gap $E_g$ is equal to 0.28, 0.30, or 0.32 eV. $E_g$ sets the value of $M$ in the TI Hamiltonian. Changes in the band gap could be practically realized through chemical or mechanical strain [34] or a different hypothetical 3D TI. The small divergence from the results for $Bi_2Se_3$ show that another 3D TI will yield $J$-$V$ characteristics similar to the ones we calculate for $Bi_2Se_3$ and the small dependence of the $J$-$V$ characteristics on the TI band gap. The peak current increases when the band gap increases from 0.28 eV to 0.32 eV. The relatively small change suggests that changing the TI of both slabs has little impact on the overall

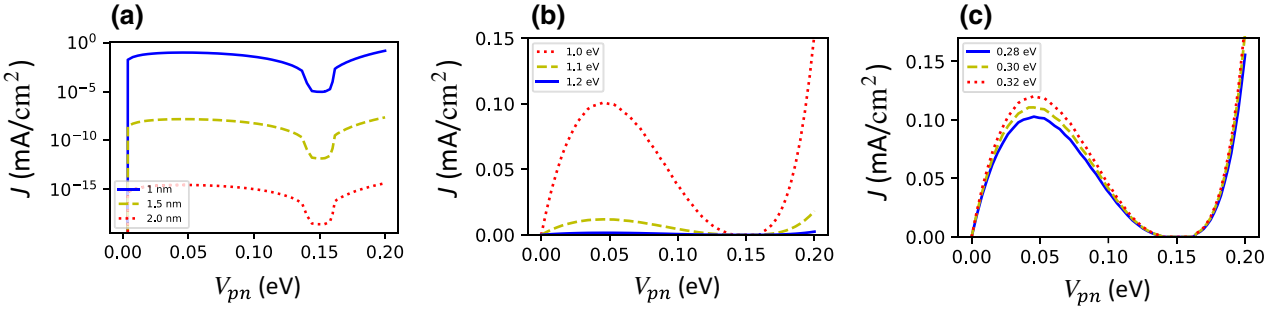


FIG. 8. (a) The current density of our proposed TI NDR device for tunnel-barrier thicknesses of $t = 1.0$ nm, 1.5 nm, and 2.0 nm. The magnitude of the current decreases while the shape remains constant as the barrier width increases. (b) The current density of the NDR device with tunnel-barrier heights of $V_{\text{onsite}} = 1.0$ eV, 1.1 eV and 1.2 eV. The magnitude of the current decreases while the shape remains constant with increasing barrier height. (c) The current density for the NDR device with band gaps $E_g = 0.28$ eV, 0.30 eV, and 0.32 eV. Changing the band gap has little impact on the current density.

current density as long as the Dirac cone is maintained in the band gap.

## IV. CONCLUSIONS

We present an NDR device based on 3D $Bi_2Se_3$ slabs sandwiching a tunnel-barrier material. The presented device utilizes the spin-momentum locking of the surface states of 3D TIs, resulting in spin-dependent tunneling. Using the Bardeen transfer Hamiltonian method, we calculate the tunneling current between the two slabs. We show that the presented NDR device, unlike conventional NDR devices, can have a valley current that is nearly zero, resulting in a very high peak-to-valley ratio. Recent devices, such as van der Waals nanostructures and InAs-GaSb core-shell nanowires [35,36] show peak-to-valley ratios of 4 [35] and 8.69 [36], respectively. This is significantly lower than the peak-to-valley ratio of our device. While the ideal system tested here presents a very low valley current, impurities in a real device may cause the current in a real device to be higher. Also, if the sample is semimetallic instead of insulating, we may also see a small amount of tunneling between the metallic states. Nevertheless, this device still has a lower valley current than other devices. The $V_{pn}$ at which the valley current occurs can be tuned by tuning the Fermi-level shift between the two slabs. We see that the peak of these $J$-$V$ curves occurs at $V_{pn} \approx \Delta E_F/3$. Moreover, we show that changing the TI material does not have a significant impact on the shape of the $J$-$V$ curve that the device produces. The two-terminal architecture of the presented 3D tunnel diodes makes our proposed device easy to manufacture [27] and to conduct experiments on, as compared to other NDR devices such as graphene nanoribbons and graphene quantum dots. The proposed device can be fabricated using molecular beam epitaxy [37–39].

## ACKNOWLEDGMENTS

This material is based upon work supported by the National Science Foundation under Grant No. 1802166. This work was supported in part by the Semiconductor Research Corporation (SRC) by the NEWLIMITS Center, and by the National Institute of Standards and Technology (NIST) through Award No. 70NANB17H041.

## APPENDIX

### 1. Calculating band structure and wave functions for a TI slab

To calculate the band structure of a TI slab, we start with the $\mathbf{k}\cdot\mathbf{p}$ Hamiltonian from Eq. (1). To obtain a slab band structure as opposed to a bulk band structure, we discretize in the out-of-plane direction by replacing $k_z$ with $-i(d/dz)$, employing the treatment described by Qi *et al.* [31]. To find the band structures numerically, we use finite differences, so that $df/dz \approx f(z+\Delta z) - f(z-\Delta z)/2\Delta z$ and $d^2f/dz^2 \approx f(z+\Delta z) - 2f(z) + f(z-\Delta z)/(\Delta z)^2$, where $\Delta z$ is the step size. In our case, we take a step size of $\Delta z = 1$ A. This leads to $n_{\mathrm{TI}} = 100$ discrete steps in the TI slab and $n_B$ =110 steps in the tunnel barrier. The systems of the $p$-doped and $n$-doped slabs are overlaid, meaning that the effective barrier size is equal to the total system size minus 2 times the TI slab size. To solve the Hamiltonian numerically, for both the slab and tunnel-barrier Hamiltonians, we take a Kronecker product of the $H_{\mathrm{TI}}$ and an identity matrix of dimensions of $100 \times 100$ for the slab and a Kronecker product of $H_D$ and identity matrix of dimensions $110 \times 110$ for the tunnel barrier. Note that prior to accounting for transitions using the Bardeen transfer Hamiltonian, when considering the $n$ slab, the $p$ slab is modeled using the tunnel-barrier Hamiltonian and vice versa.

However, since we are calculating the band structure of the slab with a connected tunnel barrier, we must combine our slab and tunnel-barrier Hamiltonians to account for a single system. We define Hamiltonians for each TI slab with a tunnel barrier as follows:

$$H_p = \begin{pmatrix} H_D & W_{T,D} \\ W_{B,\mathrm{TI}} & H_{\mathrm{TI}} \end{pmatrix}, \tag{A1}$$

$$H_n = \begin{pmatrix} H_{\mathrm{TI}} & W_{T,\mathrm{TI}} \\ W_{B,D} & H_D \end{pmatrix}. \tag{A2}$$

where Eq. (A1) is for the $p$-doped slab and Eq. (A2) is for the $n$-doped slab: Here, the numerically evaluated Hamiltonians contain the slab ($H_{\mathrm{TI}}$) and tunnel-barrier Hamiltonians $H_{\mathrm{D}}$ as the diagonal elements and connection terms $W$ as the off-diagonal elements.

The dimensions of the connection terms are $4n_{\mathrm{TI}} \times 4n_D$. The connection terms are zero matrices with the exception of four elements in the bottom-left corner for $W_{T,\mathrm{TI}}$ and $W_{T,D}$ and the top-left corner for $W_{B,\mathrm{TI}}$ and $W_{B,D}$. The exact form of $W_T$ can be seen in the following, with $W_B$ being

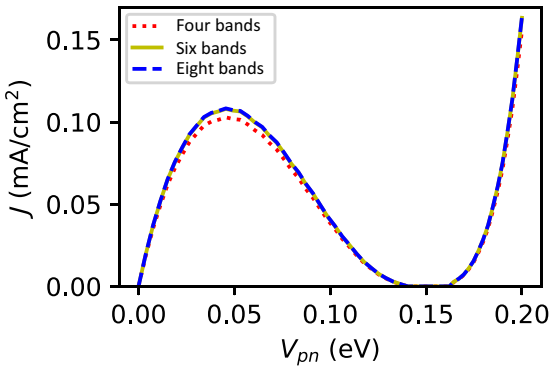


FIG. 9. The current density for a TI slab with an increasing number of calculated bands.

the adjoint of $W_T$:

$$W_T = \frac{-D_1}{(\Delta z)^2}\begin{bmatrix} 0 & \dots & \dots & \dots & \dots & \dots & 0 \\ \vdots & \vdots & \vdots & \dots & \dots & \dots & \vdots \\ \vdots & \vdots & \vdots & 0 & 0 & \dots & \vdots \\ \vdots & \vdots & 0 & 1 & 0 & \dots & \vdots \\ \vdots & 0 & 1 & 0 & \vdots & \vdots & \vdots \\ 0 & 1 & 0 & \dots & \ddots & \vdots & \vdots \\ 1 & 0 & \dots & \dots & \dots & \dots & 0 \end{bmatrix}, \quad \text{(A3)}$$

$$W_B = W_T^{\dagger}. \quad \text{(A4)}$$

### 2. Change in current density with increasing calculated bands

In Fig. 9, we can see the current density plotted for four, six, and eight bands calculated at $\Delta E_F = 0.15$ eV. We see that the magnitude of the current is affected but there is no impact on the shape. The change in current is relatively small. For a change between four bands and six bands, the maximum divergence is approximately 5%. The change in current with increasing considered bands decreases as we consider additional bands. For example, the difference in current for a calculation accounting for six versus eight bands is only approximately 0.3%.


[1] W. G. Vandenberghe and M. V. Fischetti, Imperfect two-dimensional topological insulator field-effect transistors, Nat. Commun. **8**, 1 (2017).

[2] G. Gaddemane, W. G. Vandenberghe, M. L. Van de Put, S. Chen, S. Tiwari, E. Chen, and M. V. Fischetti, Theoretical studies of electronic transport in monolayer and bilayer phosphorene: A critical overview, Phys. Rev. B **98**, 115416 (2018).

[3] C.-X. Zhao and J.-F. Jia, Stanene: A good platform for topological insulator and topological superconductor, Front. Phys. **15**, 1 (2020).

[4] X. Wang, C. Xu, H. Hu, P. Wang, G. Bian, W. Tan, S. Brown, and T.-C. Chiang, Topological phase stability and transformation of bismuthene, EPL (Europhys. Lett.) **119**, 27002 (2017).

[5] M. Z. Hasan and C. L. Kane, Colloquium: Topological insulators, Rev. Mod. Phys. **82**, 3045 (2010).

[6] S. Tiwari, M. L. V. de Put, B. Sorée, and W. G. Vandenberghe, Carrier transport in two-dimensional topological insulator nanoribbons in the presence of vacancy defects, 2D Mater. **6**, 025011 (2019).

[7] H. Wang, J. Kally, J. S. Lee, T. Liu, H. Chang, D. R. Hickey, K. A. Mkhoyan, M. Wu, A. Richardella, and N. Samarth, Surface-State-Dominated Spin-Charge Current Conversion in Topological-Insulator–Ferromagnetic-Insulator Heterostructures, Phys. Rev. Lett. **117**, 076601 (2016).

[8] W. G. Vandenberghe, C. L. Hinkle, and M. V. Fischetti, Memory devices based on gate controlled ferromagnestism and spin-polarized current injection, 3 2016. U.S. Patent 9741416B1.

[9] M. J. Gilbert, Topological electronics, Commun. Phys. **4**, 70 (2021).

[10] N. H. D. Khang, Y. Ueda, and P. N. Hai, A conductive topological insulator with large spin Hall effect for ultralow power spin-orbit torque switching, Nat. Mater. **17**, 808 (2018).

[11] A. R. Mellnik, J. S. Lee, A. Richardella, J. L. Grab, P. J. Mintun, M. H. Fischer, A. Vaezi, A. Manchon, E.-A. Kim, N. Samarth, and D. C. Ralph, Spin-transfer torque generated by a topological insulator, Nature **511**, 449 (2014).

[12] M. He, H. Sun, and Q. L. He, Topological insulator: Spintronics and quantum computations, Front. Phys. **14**, 1 (2019).

[13] M. A. Bandres, S. Wittek, G. Harari, M. Parto, J. Ren, M. Segev, D. N. Christodoulides, and M. Khajavikhan, Topological insulator laser: Experiments, Science **359**, eaar4005 (2018).

[14] H. Wu, F. Groß, B. Dai, D. Lujan, S. A. Razavi, P. Zhang, Y. Liu, K. Sobotkiewich, J. Förster, M. Weigand, G. Schütz, X. Li, J. Gröfe, and K. L. Wang, Ferrimagnetic skyrmions in topological insulator/ferrimagnet heterostructures, Adv. Mater. **32**, 2003380 (2020).

[15] Z. Wu, G. Liang, W. K. Pang, T. Zhou, Z. Cheng, W. Zhang, Y. Liu, B. Johannessen, and Z. Guo, Coupling topological insulator $SnSb_2Te_4$ nanodots with highly doped graphene for high-rate energy storage, Adv. Mater. **32**, 1905632 (2020).

[16] Z. Yang, E. Lustig, G. Harari, Y. Plotnik, Y. Lumer, M. A. Bandres, and M. Segev, Mode-Locked Topological Insulator Laser Utilizing Synthetic Dimensions, Phys. Rev. X **10**, 011059 (2020).

[17] D. Flötotto, Y. Ota, Y. Bai, C. Zhang, K. Okazaki, A. Tsuzuki, T. Hashimoto, J. N. Eckstein, S. Shin, and T.-C. Chiang, Superconducting pairing of topological surface states in bismuth selenide films on niobium, Sci. Adv. **4**, eaar7214 (2018).

[18] W. Tang, A. Politano, C. Guo, W. Guo, C. Liu, L. Wang, X. Chen, and W. Lu, Photodetectors: Ultrasensitive room-temperature terahertz direct detection based on a bismuth selenide topological insulator (Adv. Funct. Mater. 31/2018), Adv. Funct. Mater. **28**, 1870219 (2018).

[19] P. Sharma, M. Kumar, and V. Awana, Topological insulator $Bi_2Se_3$ as a tunable crystal for terahertz frequency generation, Appl. Phys. A **127**, 1 (2021).

[20] Y. Wu, D. B. Farmer, W. Zhu, S.-J. Han, C. D. Dimitrakopoulos, A. A. Bol, P. Avouris, and Y.-M. Lin, Three-terminal graphene negative differential resistance devices, ACS Nano **6**, 2610 (2012).

[21] R. Van Zyl, W. Perold, and R. Botha, in *Proceedings of the 1998 South African Symposium on Communications and Signal Processing-COMSIG'98 (Cat. No. 98EX214)*, p 407. IEEE, 1998.

[22] J. Chen, M. A. Reed, A. M. Rawlett, and J. M. Tour, Large on-off ratios and negative differential resistance in a molecular electronic device, Science **286**, 1550 (1999).

[23] H. Ren, Q.-X. Li, Y. Luo, and J. Yang, Graphene nanoribbon as a negative differential resistance device, Appl. Phys. Lett. **94**, 173110 (2009).

[24] J. M. Marmolejo-Tejada and J. Velasco-Medina, Review on graphene nanoribbon devices for logic applications, Microelectron. J. **48**, 18 (2016).

[25] P. Sharma, L. S. Bernard, A. Bazigos, A. Magrez, and A. M. Ionescu, Room-temperature negative differential resistance in graphene field effect transistors: Experiments and theory, ACS Nano **9**, 620 (2015).

[26] S. Sharma, C.-A. Cheng, S. R. M. Santiago, D. N. Feria, C.-T. Yuan, S.-H. Chang, T.-Y. Lin, and J.-L. Shen, Aggregation-induced negative differential resistance in graphene oxide quantum dots. *Phys. Chem. Chem. Phys.*, 2021.

[27] A. T. Barton, L. A. Walsh, C. M. Smyth, X. Qin, R. Addou, C. Cormier, P. K. Hurley, R. M. Wallace, and C. L. Hinkle, Impact of etch processes on the chemistry and surface states of the topological insulator $Bi_2Se_3$, ACS. Appl. Mater. Interfaces **11**, 32144 (2019).

[28] L. A. Walsh, A. J. Green, R. Addou, W. Nolting, C. R. Cormier, A. T. Barton, T. R. Mowll, R. Yue, N. Lu, J. Kim, and et al, Fermi level manipulation through native doping in the topological insulator $Bi_2Se_3$, ACS Nano **12**, 6310 (2018).

[29] H. Zhang, C.-X. Liu, X.-L. Qi, X. Dai, Z. Fang, and S.-C. Zhang, Topological insulators in $Bi_2Se_3$, $Bi_2Te_3$ and $Sb_2Te_3$ with a single Dirac cone on the surface, Nat. Phys. **5**, 438 (2009).

[30] B. J. Powell, in *Computational Methods for Large Systems: Electronic Structure Approaches for Biotechnology and Nanotechnology*, edited by J. R. Reimers (Wiley, Hoboken, NJ, United States, 2011).

[31] X.-L. Qi and S.-C. Zhang, Topological insulators and superconductors, Rev. Mod. Phys. **83**, 1057 (2011).

[32] J. Bardeen, Tunnelling from a Many-Particle Point of View, Phys. Rev. Lett. **6**, 57 (1961).

[33] M. L. Van de Put, W. G. Vandenberghe, B. Sorée, W. Magnus, and M. V. Fischetti, Inter-ribbon tunneling in graphene: An atomistic Bardeen approach, J. Appl. Phys. **119**, 214306 (2016).

[34] Y. Liu, Y. Li, S. Rajput, D. Gilks, L. Lari, P. Galindo, M. Weinert, V. Lazarov, and L. Li, Tuning Dirac states by strain in the topological insulator $Bi_2Se_3$, Nat. Phys. **10**, 294 (2014).

[35] S. Fan, Q. A. Vu, S. Lee, T. L. Phan, G. Han, Y.-M. Kim, W. J. Yu, and Y. H. Lee, Tunable negative differential resistance in van der Waals heterostructures at room temperature by tailoring the interface, ACS Nano **13**, 8193 (2019).

[36] C.-W. Hsu, Q. H. Luc, P. Huang, J. Y. Wu, N. A. Tran, and E. Y. Chang, *et al.*, in *ECS Meeting Abstracts*, no. 51, p. 3835. IOP Publishing, 2020.

[37] M. A. Herman and H. Sitter, *Molecular Beam Epitaxy: Fundamentals and Current Status* Vol. 7 (Springer Science & Business Media, Springer-Verlag Berlin, 2012).

[38] Y. R. Sapkota, *Physical Properties of Topological Insulator: Bismuth Selenide Thin Films*. Southern Illinois University at Carbondale, 2017.

[39] L. A. Walsh and C. L. Hinkle, Van der Waals epitaxy: 2D materials and topological insulators, Appl. Mater. Today **9**, 504 (2017).